EFFECTS OF FAVORABLE DOWNSTREAM PRESSURE GRADIENTS ON SEPARATED SHOCK-WAVE/BOUNDARY-LAYER INTERACTIONS

Lionel Larchevêque
Aix-Marseille Univ, CNRS, IUSTI
Marseille, France
lionel.larcheveque@univ-amu.fr

Deepak Prem Ramaswamy,
Institute of Aerodynamics and Chair of Fluid Mechanics
RWTH Aachen University
52062 Aachen, Germany
d.ramaswamy@aia.rwth-aachen.de

Anne-Marie Schreyer,
Institute of Aerodynamics and Chair of Fluid Mechanics
RWTH Aachen University
52062 Aachen, Germany
a.schreyer@aia.rwth-aachen.de

ABSTRACT

Shock-wave/boundary-layer interactions (SWBLI) strongly influence the aerodynamic behavior of many aerospace- transportation systems. They have therefore been studied intensively – with different methods, configurations, and test facilities. Regions of favorable pressure gradient are often placed downstream of the SWBLI region. To be able to better understand their effect and compare cases from varying sources, a joint experimental–numerical study of a supersonic compression/expansion corner flow is carried out. A High–resolution long–time numerical simulation complements particle-image velocimetry measurements, both using the same configuration and conditions. Derived setups without the downstream expansion corner are also explored; both for the same compression-corner angle and for a ramp angle inducing a separation bubble of the same size as for the original compression/expansion configuration. It is shown that the topology and low–frequency dynamics of the separation bubble developing over the compression corner are altered by the downstream expansion. POD analyses show that the geometrical constraint downstream of the interaction region results in a shortening of the “natural” modes but also in the merging of several modes, altering their time evolution.

INTRODUCTION

Regions of favourable pressure gradient are often located downstream of shock-wave / boundary-layer interaction (SWBLI), either by design for practical devices such as air intakes or to prevent unstart of supersonic wind tunnels. If the favourable pressure gradient is located in the close vicinity of a separated SWBLI, it may alter the size of the separation bubble, as documented for instance experimentally by Grossman & Bruce (2018) or numerically by Duan *et al.* (2021). Several studies have also documented the frequency content in the favourable pressure gradient region, see for instance Grilli *et al.* (2013) or Duan *et al.* (2021).

However, little attention has been paid to the frequency link between the SWBLI and the favourable pressure gradient regions. Moreover, as far as the authors know, any possible effects induced by the downstream pressure gradient on the low–frequency dynamics of the separation bubble have not yet been documented. The present study aims at closing this gap in knowledge by jointly analyzing the experimental data of a $M_\infty = 2.52$, 24° compression-corner interaction followed by -24° expansion corner of Ramaswamy & Schreyer (2021) with high-resolution large–eddy simulations (LESs).

We first computed the same compression corner–expansion corner configuration as studied in the experiments. This baseline computation is hereafter labeled as c24.0-e24.0. Two additional computations with a single compression corner were also carried out. The first one uses the same 24° corner as the baseline case, while the corner angle has been reduced to 21.7° for the second case to obtain the same separation location as in the c24.0-e24.0 case. These two computations are labeled c24.0 and c21.7, respectively.

EXPERIMENTAL AND NUMERICAL SETUP
Experiments

Experimental investigations were conducted in the trisonic wind tunnel at RWTH Aachen University. The intermittently-operating vacuum-storage facility achieves stable run times of 3–4 s. Air as the working fluid is supplied to a settling balloon. The air is dried to avoid condensation effects, keeping the relative humidity below 6%. The $0.4 \times 0.4\,\mathrm{m}^2$ test section is optically accessible through two circular windows on either side of the test section and one on the top wall. The ambient conditions listed in Tab. 1 set the wind-tunnel stagnation conditions. The selected Mach number ($M_\infty = 2.52$) therefore determines the free-stream unit Reynolds number ($Re_\infty = 9.6 \cdot 10^6\, 1/m$).

For the two-component particle-image velocimetry (PIV) measurements, we used a 532 nm Litron NANO-L pulsed PIV laser with a maximum pulse energy of 200 mJ to illuminate the di-ethyl-hexyl-sebacate seeding particles in the flow. Two FlowSense EO 11M cameras (equipped with 4008 px×2672 px CCD sensors and Tamron SP AF 180mm f/3.5 objectives) covered the same field of view, the complete SWBLI region ($-4.5\delta \leq x \leq 4.5\delta$; $\delta = 10.4\,\mathrm{mm}$ is the in-

Table 1. Flow parameters

M_∞	P_0 (Pa)	T_0 (K)	Re_θ	δ (mm)
2.52	9.949×10^4	297	8225	10.4

Table 2. Simulation parameters

Case	Span	Cells	LF cycles
c24.0-e24.0	3.5δ	87 M	145
c24.0	7.4δ	181 M	55
c21.7	3.5δ	87 M	90

coming boundary-layer thickness), at a spatial resolution of 43 px/mm. The cameras were triggered alternately to increase the overall acquisition rate to 6 Hz.

Large-eddy simulations

All computation were carried out using the FLU3M code with second–order accuracy both in time and space. Time integration is implicit with a typical maximum CFL number of 11. The space scheme is hybrid centred–shock capturing discriminated by the Ducros' sensor. The explicit subgrid scale modelling relies on the selective mixed–scale model. A compressible variant of the synthetic eddy method (SEM) is used to generate unsteady fully turbulent inflow boundary condition. The inflow boundary is located 16δ upstream of the separation corner for all computations in order to ensure a similar development of the incoming boundary layer regardless of the extent of the interaction region.

For more details on the numerics see Jiang *et al.* (2017); we derived the present mesh parameters from their study: for all computations, the inflow is located more than 10δ upstream of the interaction region and the width of the computational domain is set larger than 7 separation–bubble heights. The size of the bubble varies between the cases, resulting in different extensions in the spanwise direction. The total cell counts range between 87 and 181 millions, as shown in table 2.

The typical grid resolutions in wall units are set to $\Delta x^+ = 26.5$ and $\Delta z^+ = 10.5$. In the wall-normal direction, the mesh has a typical stretching rate of 3%, starting from $\Delta y^+_{wall} = 0.7$ with 170 cells within the boundary-layer thickness. The body–fitted mesh is built using numerical conformal mapping.

All simulations have been run for 2.2 millions time steps, thus providing data sampled over a physical duration of 0.22 s. The corresponding number of typical low–frequency cycles distributed over this duration varies, but is over 50 for all computations (see Tab. 2). This run time ensures good statistical convergence for all spectral estimators in all cases.

Validation

The mean-velocity and Reynolds-stress profiles feeding the SEM boundary conditions have been obtained from a preliminary LES of a $M_\infty = 2.52$ flat–plate boundary layer undergoing transition. The location at which these profiles have been sampled has be adjusted so that the SWTBLI computation matches the boundary-layer parameters listed in Tab. 1 at location $x/\delta = -4.3$. The resulting boundary-layer thickness

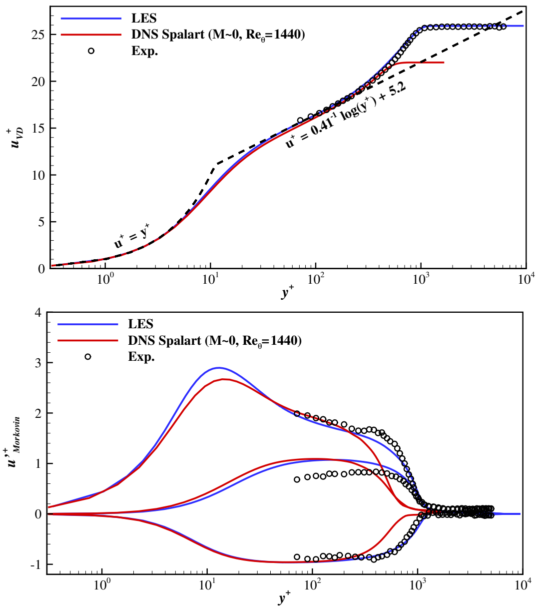

Figure 1. Van Driest–transformed streamwise velocity profiles in wall unit (top) and velocity fluctuation profiles in Morkovin Scaling (bottom) at location $x/\delta = -4.3$

and skin friction differ by less than 3% from the experimental values and the overall profiles are in very good agreement (see Fig. 1). The main discrepancy is in the streamwise fluctuation profile above the log layer: the LES fails to reproduce the secondary peak associated with very large structures that is emerging in the experiments due to the high Reynolds number. The reason for this difference is that the inflow boundary is located $\mathcal{O}(10\delta)$ upstream of the sampling station, *i.e.* not far enough for structures with a larger length scale to sustain.

Next, we compare the PIV and the LES data for the reference case c24.0-e24.0. The global structure of the compression/expansion corner flow, visualized using the isolevels of the streamwise velocity and streamlines, is shown in Fig. 2. The LES accurately reproduces all flow features from the separation point to the relaxation region downstream of the reattachment – which is significantly altered by the expansion corner. The most noticeable discrepancy between experiment and simulation is an underestimation by about 7% of the extent of the separated region by the latter.

Such small differences in length can easily be compensated by rescaling the separated region with the actual interaction length, defined as the distance between the corner and the extrapolation of the head shock down to the wall. The relaxation region downstream of the reattachment, however, scales more naturally with the distance between the compression and expansions corners, which is identical for the experiments and the computation. The dual–lengthscale dependence is taken into account by considering a composite reference lengthscale for the computation: in the separated region, the interaction length is considered. Downstream, from the reattachment point to the expansion corned, the length scale is increased linearly to match the the experimental interaction length at that location.

This way, the usual normalization is considered for the interaction region, and we are able to recover the same normalized location of the expansion corner in both the experiments and the LES.

The normalized streamwise evolution of the mean and fluctuating velocity profiles is plotted in Fig. 3. It is clearly

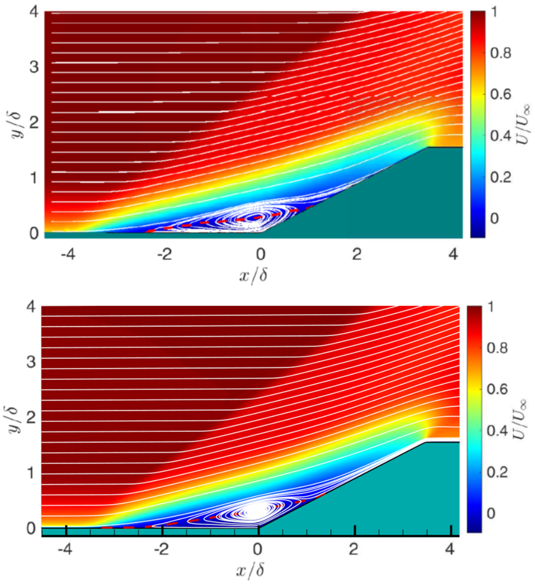

Figure 2. Isocontour of streamwise velocity with superimposed streamlines. The red dashed line dénotes the 0-isolevel of streamwise velocity; PIV measurements (top) and LES simulation (bottom).

visible that the LES accurately reproduces the flow developing over the compression corner–expansion corner geometry. The most noticeable difference occurs once again in the streamwise velocity fluctuation profiles in Fig. 3(b), where the peak level at the heart of the mixing layer developing over the separated region is underestimated by about 15%. Such an underestimation was already observed in Jiang *et al.* (2017) and was traced back through spectral analyses to the lack of very large structures in the incoming boundary layer. The same explanation most probably holds here.

The validation process can be expanded to gain further information on the flow dynamics by comparing the Proper Orthogonal Decomposition (POD) of the 2D (u,v) velocity fields obtained from the experiments and the LES. POD has been computed using the snapshot method from 782 snapshots with a sampling rate of 6 Hz (experiments) and 88000 snapshots with a sampling rate of 400 kHz (LES). Note that the highest available sampling rate has been used in the latter case to make it possible to compute spectral estimates from the temporal modes over the full frequency range. Maps of normalized 2D turbulent kinetic energy are plotted in Fig. 4 for the six most energetic modes found in the experiments (left column) or the c24.0-e24.0 LES (center column).

The relative energy contents of the modes are also reported in Fig. 4. The modes obtained from the experiments are carrying relatively more energy than their numerical counterparts. This difference may be explained with the differing spatial extents of the domain over which the inner product is computed in the experiments and the numerical simulation (the upstream and downstream bounds of the experimental field of view are denoted by dashed line onto the LES map). Moreover, levels of normalized turbulent kinetic energy (obtained by dividing the unnormalized space modes by their respective eigenvalues) are lower for the experiments than for the simulation (see Fig. 4). Hence, the unnormalized fluctuations associated with each mode are similar in absolute energy content.

The two first modes are similar in the experiments and the LES, demonstrating that the dominant dynamics of the flow

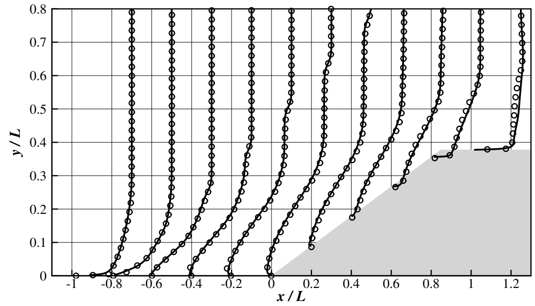

(a) $\overline{u}$

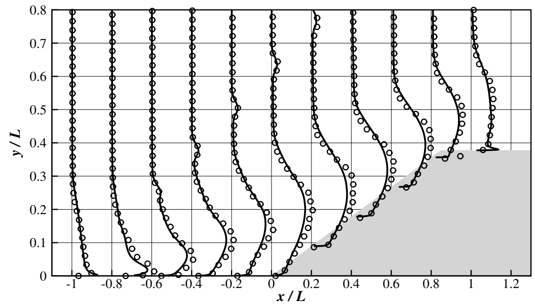

(b) u'

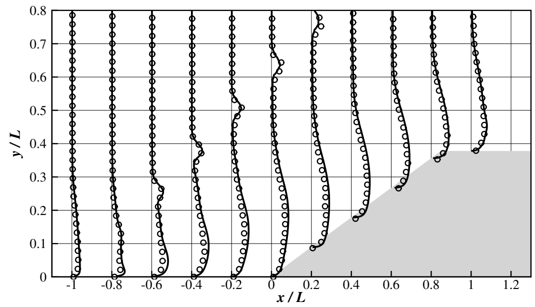

(c) v'

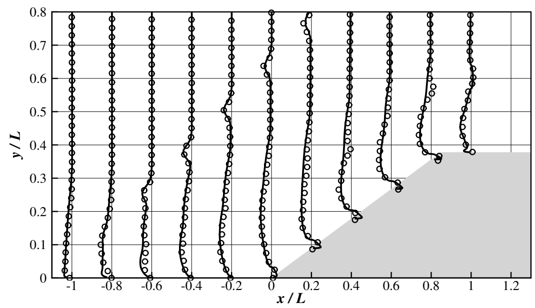

(d) $\mathrm{sign}(u'v') \times \sqrt{|u'v'|}$

Figure 3. Streamwise evolution of the velocity profiles along the interaction region: PIV measurements (○) and c24.0-e24.0 LES (——).

are well predicted by the simulation. The third modes sightly differ in the location of the intermediate structure. This is most probably caused by the slight difference in size of the separated region between the experiments and the computation, considering that the mode is driven both by the (variable) size of the separation bubble and the (fixed) extent of the ramp.

Higher-order modes significantly differ. They occasionally bear a resemblance in the separated region, but differ further downstream. This behavior is possibly due to the difference in the separation length/ramp length ratio: compare for instance modes 6 from the experiment and mode 5 from the

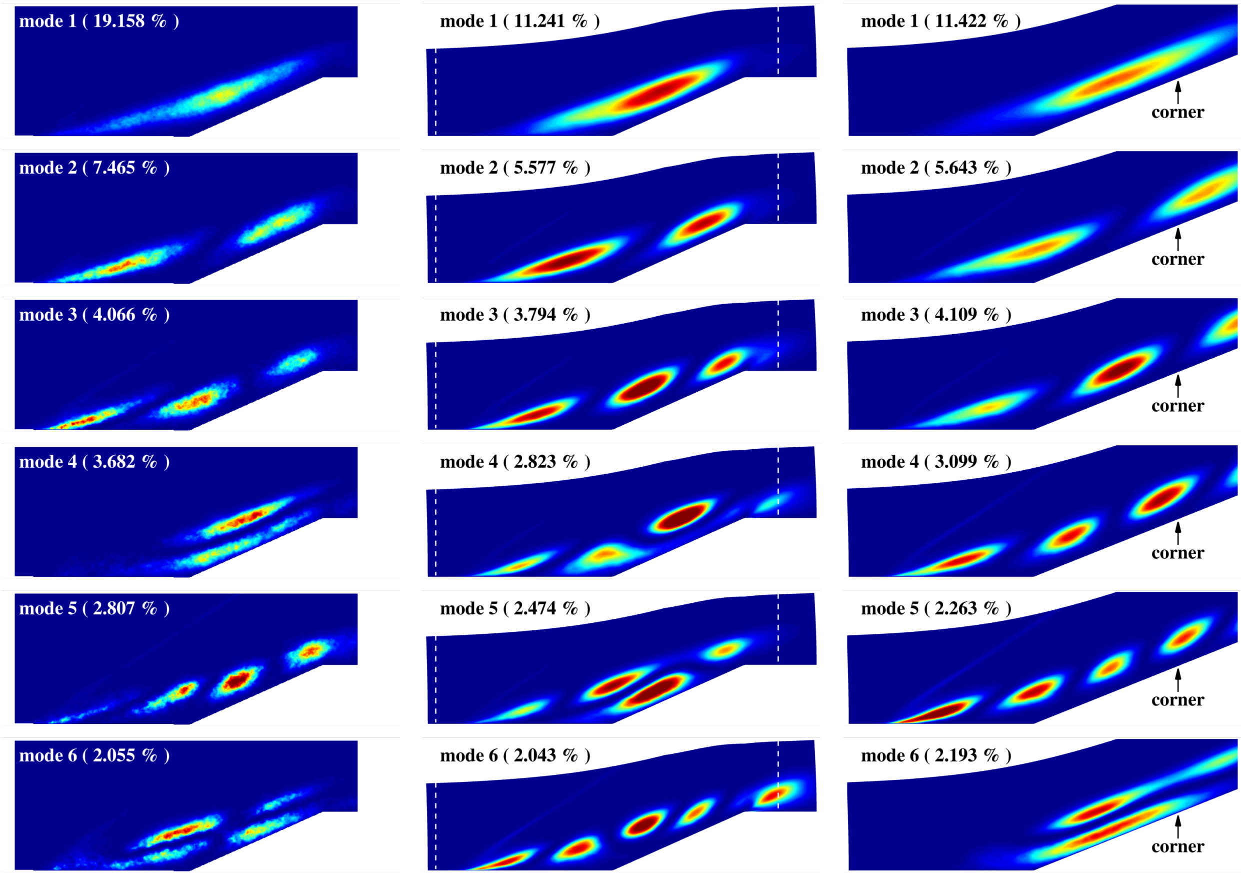

Figure 4. Isocontours of the 2D turbulent kinetic energy for normalized POD modes obtained from snapshots of streamwise and wall–normal velocities: experiments (left), c24.0-e24.0 LES (middle) and c21.7 LES (right).

numerical simulation. We will show that the corner indeed induces compression as well as truncation in space for the modes at the end of the next section.

RESULTS AND DISCUSSION

Equivalent compression corner flows

Comparing the c24-e24 computations with the two other computations, for which the downstream expansion corner has been removed, helps assessing the influence of the downstream favourable pressure gradient on the separated region. The skin-friction and wall-pressure coefficient distributions are displayed in Fig. 5 for the three computations. They demonstrate that case c21.7 (reduced ramp angle) indeed results in the same separation location as the c24.0-e24.0 case, but that the lack of a downstream favourable pressure gradient leads to a slightly delayed reattachment. In contrast, the c24.0 case exhibits a very large separation region inducing a true pressure plateau. The expansion corner in the nominal setup has indeed a significant impact on the mean development of the SWTBLI, leading to a shrinking of the separation bubble by more than 30%.

Spectral analysis

On the basis of the scaling well acknowledged for turbulent SWBLIs (Dupont *et al.* (2006)), we expected that the c24.0-e24.0 and c21.7 cases would exhibit similar low frequency dynamics (associated with the breathing of the separated region), since they have the same interaction lengths. Such dynamics are indeed evidenced by the wall pressure spectrum near the separation point. Standard turbulent SWBLIs exhibit a clustering of the low–frequency power around a Strouhal number based on the length of the interaction region of $St_L \simeq 0.03$, and both the c21.7 and c24.0 cases exhibit such

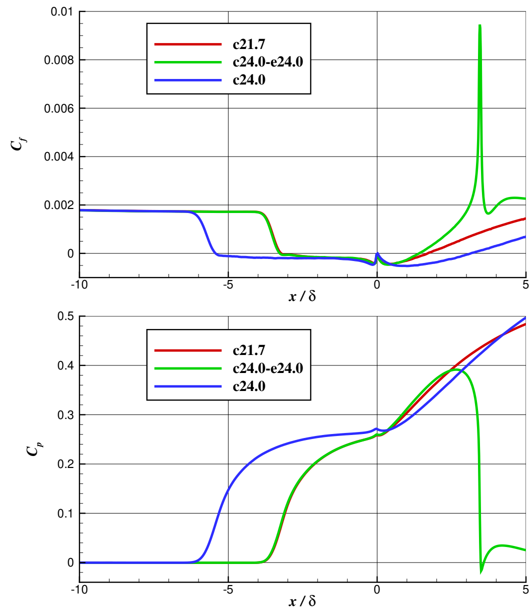

Figure 5. Distribution of the skin friction coefficient (top) and wall pressure coefficient (bottom) for the three LESs.

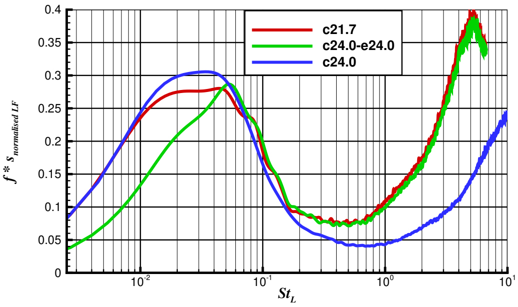

Figure 6. Normalized wall pressure power spectra at the beginning of the interaction region ($x^* = 0$).

a clustering (see Fig. 6).

The c24.0-e24.0 case, however, has a narrower low frequency distribution whose centre is shifted up by 50% because of the disappearance of the energy content in the lower part of the low–frequency range. The lack of dynamic content at the lowest frequencies persists until the region downstream of the expansion corner, as seen in the center plot of Fig. 7.

The streamwise distribution of the norm of the wall pressure cross–spectrum between the current location and the beginning of the interaction, normalised by the local pressure variance to highlight the energetically prevailing linear coupling, is dominated by the frequency range over $St = 0.03$ (denoted by the horizontal dashed line). The single corner cases, on the other hand, exhibit significant linear coupling for frequencies below $St = 0.03$ downstream of the corner (located at $x^* = 1$), as visible in the upper and lower maps of Fig. 7.

Proper orthogonal decomposition

Although the low-frequency dynamics of the separated region appear to be significantly affected by a downstream favourable gradient exerted by the expansion corner, it is unclear how this gradient modifies the frequency–space structure of the interaction and downstream relaxation regions. Therefore, we computed time-resolved POD modes for the c21.7 case to complement the corresponding POD modes for the c24.0-e24.0 LES as a first attempt to relate flow entities coherent in space with given frequency distributions.

Turbulent kinetic energy maps for the six first modes obtained from the c21.7 computation are plotted in the right column of Fig. 4. The three first modes appear to be elongated versions of the three first modes of the c24.0-e24.0 case, while modes 5 and 6 look similar to modes 5 and 4 in the experiments. It should, however, be considered that modes 2, 3 and 4 of the c21.7 case have to be associated with modes 1, 2 and 3 of the c24.0-e24.0 case. This illustrates the difficulty to match the c21.7 and c24.0-e24.0 modes; it is challenging to infer the kind of distortion in space induced by the expansion corner.

To identify partial dynamics common to both cases, a joint POD encompassing snapshots from both the c21.7 and c24.0-e24.0 LESs with the same full sampling rate has been computed. As expected, modes obtained from the diagonalization of the time-correlation matrix are mostly dominated by fluctuations associated with one or the other of the single flow cases and match the ones obtained when a single datadase is considered (see Fig. 4). Most often, however, flow patterns can also be identified for the other case, yet with much lower energy. These "ghosts" are related to the flow patterns of another mode, highlighting common dynamics.

Based on this methodology, modes 1 to 3 of the c24.0-e24.0 case are more likely related to modes 2 to 4 of case c21.7,

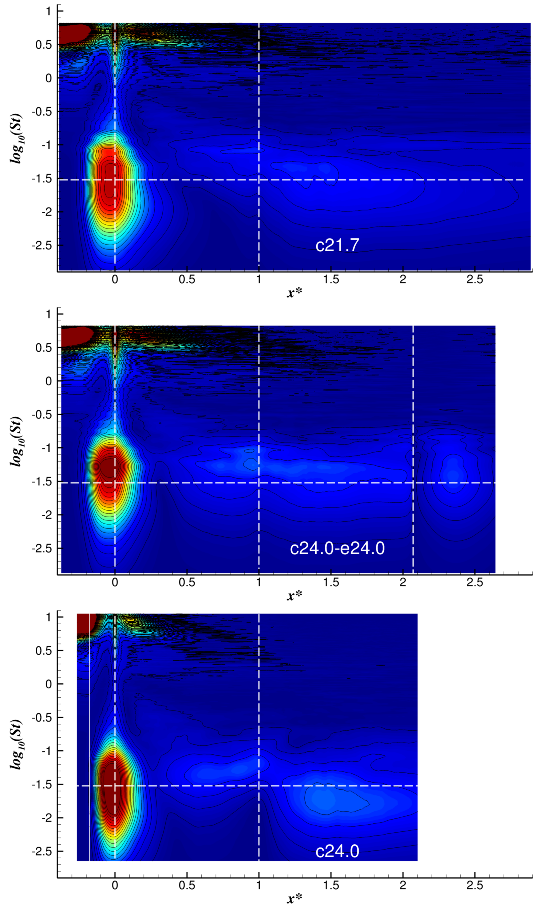

Figure 7. Streamwise distribution of the normalized cross-spectrum between the local pressure and the pressure at location $x^* = 0$ for the three LES computations.

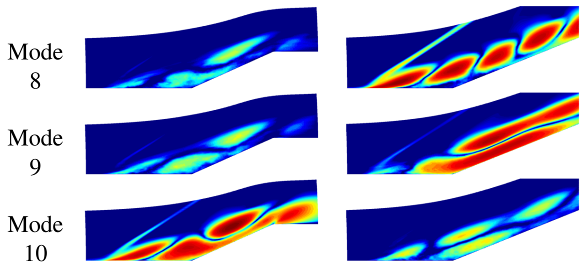

Figure 8. Isocontour of 2D turbulent kinetic energy from various modes of the joint POD: c24.0-e24.0 plane (left) and c21.7 plane (right).

especially for the latter pairs. Moreover, the approach allows to clearly point out that the expansion corner causes modes 5 and 6 of the c21.7 computation (corresponding to modes 8 and 9 in the joint POD) to merge into the composite mode 4 (mode 10 in the joint POD), as evidenced in Fig. 8. "Ghosts" of case c24.0-e24.0 in joint modes 8 and 9 have the same structure in space as mode 10, whereas the "ghost" of the c21.7 LES for mode 10 appears to be a blend of modes 8 and 9. These findings may explain the previous observation that no mode obtained from the experiments matches the c24.0-e24.0 mode 4, whereas c21.7 modes 5 and 6 have matching experimental counterparts. The length scales of the latter two modes, whose length naturally scales with the size of the separation bubble, are compatible with the extent of the compression ramp in

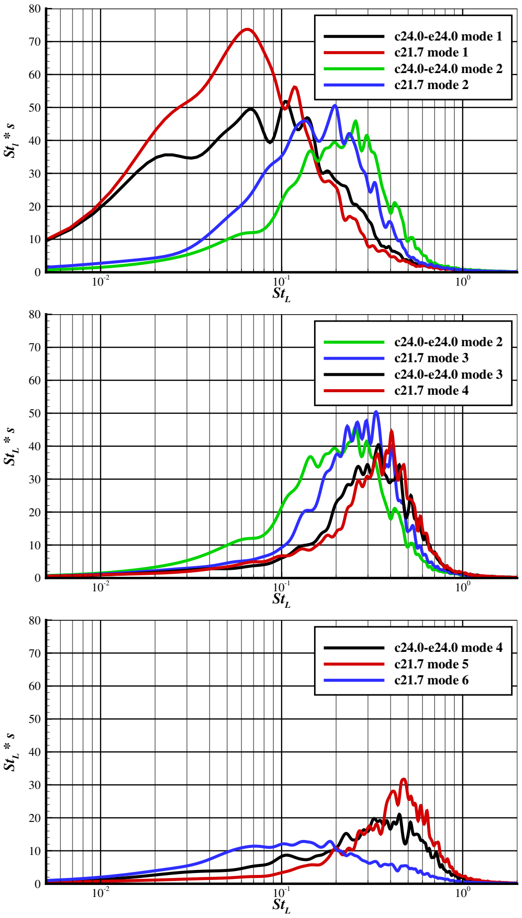

Figure 9. Premultiplied power spectrum of the first POD modes for the c24.0-e24.0 and c21.7 LES.

the experiments. For c24.0-e24.0, the slightly reduced length-scale, due to the reduced separation length, is no longer compatible with the unchanged extent of the compression ramp, and modes cannot be sustained without merging.

Once the links between modes have been identified, it is possible to study their temporal behaviour by analyzing the power spectra obtained from the temporal modes. Spectra obtained for the dominant modes are plotted in Fig. 9. The upper plot shows that modes 1 for both computations have a similar frequency distribution and therefore cannot account for the difference in the low-frequency region seen in Fig. 6. Modes 2 exhibit an upper phase shift between c21.7 and c24.0-e24.0 that could be compatible with what is seen in Fig. 6 but, as mentioned previously c24.0-e24.0 mode 2 has more likely to be related to c21.7 mode 3.

Indeed, as seen in the middle plot of Fig. 9, the frequency range associated with c24.0-e24.0 mode 2 has a slightly better match c21.7 mode 3 than with c21.7 mode 2, while the frequency ranges of the c24.0-e24.0 mode 3 and c21.7 mode 4 overlap almost perfectly. Lastly, the frequency distribution of c24.0-e24.0 mode 4 is a mix of the distributions of the two related modes of the c21.7 case. A net power loss results in the low–frequency range for the c24.0-e24.0 single mode compared to the c21.7 pair of modes.

The lack of the lowest frequency range in the c24.0-e24.0 case thus appears to result from a shift of the POD modes towards higher frequencies, from the disappearance of low–frequency dominated modes or from a combination of the two. Further refined analyses are required to clarify that point.

CONCLUSION AND FUTURE WORKS

A joint experimental/numerical study has highlighted that a favourable downstream pressure gradient alters the low-frequency dynamics of a separated SWBLI beyond the frequency scaling associated with a change in size of the separated region.

Comparison of PODs obtained for computations with and without the downstream expansion corner demonstrated that the corner induces distortions of the modes, either by contracting them or by merging several modes. It is still unclear, by which of these mechanisms the presence of the expansion corner results in the depletion of the very–low energy content.

Refined modal decompositions, more targeted towards the frequency space, such as a linear stochastic estimation built from the correlation between the wall pressure time series and the time coefficients of the POD modes or a spectral POD could help refine the analysis of the link between the low-frequency breathing of the separated bubble and the downstream relaxation region. Dynamic-mode decomposition applied to the Schlieren-image sequences (see Schauerte & Schreyer (2018)) and a similar analysis applied to the LES databases may also prove helpful.

ACKNOWLEDGMENTS

This work was granted access to the HPC resources of IDRIS under allocations A0062A01877, A0082A01877 and A0102A01877 made by GENCI.

This research was partially funded by the German Research Foundation DFG (Emmy Noether Programme, grant SCHR 1566/1-1).

REFERENCES

Duan, J., Li, X., X. Li, Xinliang & Liu, H 2021 Direct numerical simulation of a supersonic turbulent boundary layer over a compression–decompression corner. *Physics of Fluids* **33** (6), 065111.

Dupont, P., Haddad, C. & Debiève, J. F. 2006 Space and time organization in a shock-induced separated boundary layer. *Journal of Fluid Mechanics* **559**, 255–277.

Grilli, M., Hickel, S. & Adams, N. A. 2013 Large-eddy simulation of a supersonic turbulent boundary layer over a compression–expansion ramp. *International Journal of Heat and Fluid Flow* **42**, 79–93.

Grossman, I. J. & Bruce, P. J. K. 2018 Confinement effects on regular–irregular transition in shock- wave–boundary-layer interactions. *Journal of Fluid Mechanics* **853**, 171–204.

Jiang, T., Schreyer, A.-M., Larchevêque, L., Piponniau, S. & Dupont, P. 2017 Velocity spectrum estimation in shock-wave/turbulent boundary-layer interaction. *AIAA Journal* **55** (10), 3486–3498.

Ramaswamy, D. P. & Schreyer, A.-M. 2021 Control of shock-induced separation of a turbulent boundary layer using air-jet vortex generators. *AIAA Journal* **59** (3), 927–939.

Schauerte, C. & Schreyer, A.-M. 2018 Design of a high-speed focusing schlieren system for complex three-dimensional flows. In *Proceedings of the 5th International Conference on Experimental Fluid Mechanics*, pp. 232–237.